BIAS VOLTAGE IN FINITE LENGTH, CYLINDRICAL AND COAXIAL RF DISCHARGES

by

M. A. Lieberman and S. E. Savas

Memorandum No. UCB/ERL M89/121

9 October 1989

BIAS VOLTAGE IN FINITE LENGTH, CYLINDRICAL AND COAXIAL RF DISCHARGES

by

M. A. Lieberman and S. E. Savas

Memorandum No. UCB/ERL M89/121

9 October 1989

ELECTRONICS RESEARCH LABORATORY

College of Engineering
University of California, Berkeley
94720

BIAS VOLTAGE IN FINITE LENGTH, CYLINDRICAL AND COAXIAL RF DISCHARGES

by

M. A. Lieberman and S. E. Savas

Memorandum No. UCB/ERL M89/121

9 October 1989

ELECTRONICS RESEARCH LABORATORY

College of Engineering
University of California, Berkeley
94720

BIAS VOLTAGE IN FINITE LENGTH, CYLINDRICAL AND COAXIAL RF DISCHARGES

M.A. Lieberman

Department of Electrical Engineering and Computer Sciences

and the Electronics Research Laboratory

University of California, Berkeley, CA 94720

and

S.E. Savas

Applied Materials, Inc.

Santa Clara, CA 95054

ABSTRACT

We obtain the ratio V_a/V_b of the d.c. glow-to-electrode voltages at the powered (a) and grounded (b) electrodes in low pressure capacitive r.f. discharges having unequal electrode areas A_a and A_b in finite length cylindrical and coaxial geometry. We use a transport model in the glow in which ions are generated by thermal electron ionization and are lost by ambipolar diffusion in the glow, with a constant diffusion coefficient. Three electrode sheath models are considered: collisionless ions, collisional ions with a constant mean free time, and collisional ions with a constant mean free path. Using these and the continuity of the r.f. current flow, we obtain the voltage ratio as a function of the electrode area ratio, the length-to-radius ratio of the cylinder, and, for coaxial systems, the ratio of inner-to-outer radii. The theory is in good agreement with experiments[1-4] in cylindrical and coaxial geometry.

1. K. Kohler, J.W. Coburn, D.E. Horne, E. Kay, and J.H. Keller, *J. Appl. Phys.* 57, 59 (1985).

2. J.W. Coburn and E. Kay, *J. Appl. Phys.* 43, 4965 (1972).

3. C.M. Horwitz, *J. Vac. Sci. Technol. A* 1, 60 (1983).

4. G.Y. Yeom, J.A. Thornton, and M.J. Kushner, *J. Appl. Phys.* 65, 3825 (1989).

I. INTRODUCTION

Capacitive, radio frequency (r.f.) discharges are widely used for materials processing in the electronics industry. Typical parameters are pressure $p \approx 10$–300 mTorr, $\omega/2\pi \approx 13.56$ MHz, voltage $V_{rf} \approx$ 50-1000 V, and electrode spacing $l \approx 3$–10 cm. The discharges are generally asymmetric; ie, the powered electrode a and the grounded electrode b have different areas, with A_a typically less than A_b. This asymmetry determines the magnitude of the self-bias voltage V_a (the ion bombarding energy) at the powered electrode, which is a critical process parameter. Simple arguments[1] assuming equal ion current density to the two electrodes yield the scaling of the voltage ratio on the area ratio as $V_a/V_b = (A_b/A_a)^4$, contrary to measurements[1–9] that indicate a much weaker dependence of V_a/V_b on A_b/A_a for area ratios much different from unity. Pointu[10] has formulated an analytical model for the sheath voltage ratio, based on probe theory, which includes the effect of the floating potential and better fits some of the experiments[6]. In this, she assumes collisionless sheaths and equal ion current densities at electrode surfaces. One dimensional spherical shell models have also been developed[11,12], incorporating various assumptions for the sheath and glow physics, and obtaining a scaling more in agreement with measurements. However, the measurements are generally done in finite cylindrical, coaxial, or more complicated geometries having two or more dimensionless geometry parameters; e.g., the powered-to-grounded area ratio and the length-to-radius ratio for a finite length cylinder. In principle, the voltage ratio depends on all the parameters, and, therefore, there may be no simple scaling with the area ratio alone. In this work, we show that this is indeed the case. From general principles, we derive the voltage ratio in terms of the ratio of two integrals over the powered and grounded areas, which depend on the density at the plasma-sheath edge. We introduce various models for the sheath physics, from which we determine the scaling of the voltage ratio with the discharge geometry parameters. Finally, we compare our results with measurements in systems that closely approximate the model geometries.

In the model, we assume that almost all the applied r.f. voltage is dropped across thin sheaths, having thicknesses s_a and s_b, at the powered and grounded electrodes. In the pressure regime of interest, the ion-neutral mean free path λ_i may be short compared to s_a and s_b. For example, in an argon discharge $\lambda_i \approx (200\,p)^{-1}$ cm; for $s \approx 1$ cm, we obtain $\lambda_i \lesssim s$ for $p \gtrsim 5$ mTorr. It follows that

the assumption of collisionless ion transport in the sheath, which leads to a Child law scaling[13] for the ion current density, $J \propto V^{3/2}/s^2$, is usually valid only at the lowest pressures. Cobine[14] gives the scaling $J \propto V^2/s^3$ for constant ion mobility, such that the ion mean free time τ_i is constant. This models ion transport in the sheath due to ion-neutral elastic scattering. However, charge transfer of the ion with the parent neutral gas atom can also contribute to the ion transport in the sheath. This resonant process has a cross section, and therefore a mean free path, that is roughly a constant, independent of the ion drift velocity u. Because u varies within the sheath, $\tau_i \simeq \lambda_i/u$ is not a constant. In this work, we obtain the voltage ratio for these three ion transport assumptions. The gas species and pressure determine which assumption is most reasonable physically for a particular discharge.

We also assume that the glow region between the sheaths, having a thickness $d \gg s$ serves to maintain the discharge by means of the balance between ion generation there and loss to the electrodes. We assume that the electron temperature T_e in the glow is uniform, and the volume ionization rate is $\nu_{iz} n$, where ν_{iz} is the ionization frequency and n is the electron density. Secondary electrons and local ionization near the sheaths are important at high pressures and can also contribute to the ionization, but we do not consider these mechanisms here[11]. Ions are lost by ambipolar diffusion to the two electrodes. We consider a simple, constant mean free time process that models ion-neutral elastic scattering, yielding a constant diffusion coefficient D. The processes of ionization and diffusion determine the plasma density profile and, in particular, the densities at the two sheath edges near the powered and grounded electrodes, which are not equal as is so often assumed. In turn, these densities determine the sheath properties and thus the sheath voltages V_a and V_b.

The separation into distinct sheath and glow regions is somewhat arbitrary. We use the Bohm sheath criterion[15] to define the plasma-sheath edge; i.e., the diffusion solution in the glow is assumed to be valid only for $u < u_B$, where $u_B = (eT_e/M)^{1/2}$ is the Bohm (ion sound) velocity, e/M is the ion charge-to-mass ratio, and T_e is in units of volts. The plasma-sheath edge is thus the surface (near the discharge walls) where $u = u_B$.

II. BASIC THEORY

The discharge configurations are shown in Fig. 1. In Figs. 1(a)-(c), the discharge occurs in a right circular cylinder of radius R and length L. Figure 1(a) shows the geometry of Coburn and Kay[7]. The powered electrode is a disk $r < R_a$ at the cylinder bottom. The grounded electrode consists of the annulus $R_a < r < R$ at the bottom and the disk $r < R$ at the top. The sidewall is assumed to be a thick insulator that is an open circuit to the r.f. current flow. Figure 1(b) shows the geometry of Horwitz[8]. The powered electrode is the bottom disk $r < R$ and the bottom part of the sidewall $-L/2 < z < H-L/2$. The grounded electrode is the remainder of the cylinder surface. Figure 1(c) shows the geometry of Kohler et al[6], for which the entire sidewall is part of the grounded electrode. Finally, Fig. 1(d) shows a typical coaxial geometry, such as used by Yeom et al[9]. Here, the powered (grounded) electrode is the inner (outer) coaxial conductor of radius R_i (R_o) and length L, and the end surfaces are part of the grounded electrode. In all cases, a small gap is assumed to separate adjacent powered and grounded surfaces.

To derive the fundamental scaling formula, we let $\bar{x}$ be a two dimensional vector that specifies the position on the electrode surface, $n_s(\bar{x})$ be the density at the plasma-sheath edge, $V(\bar{x})$ be the d.c. glow-to-electrode voltage, $s(\bar{x})$ be the sheath thickness, and $J(\bar{x})$ be the r.f. current density normal to the electrode surface. A key observation is that the glow, being highly conducting, cannot support a potential difference greater that a few T_e's. Since $V \gg T_e$, the plasma-sheath edge is an equipotential surface. Since each electrode a and b is also an equipotential surface, the glow-to-electrode voltage across each sheath is a constant, independent of the position $\bar{x}$ along the surface. For the powered electrode, we therefore have $V_a(\bar{x}) = V_a = \text{const.}$

The relation between the r.f. voltage amplitude $\tilde{V}_a$ and the d.c. voltage drop V_a is complicated[16]. An approximate form is[17]

$$V_a = T_e \ln [I_o(\tilde{V}_a/T_e)] - (T_e/2) \ln (M/2\pi m) , \tag{1}$$

where T_e is the electron temperature (in units of volts) and M/m is the ion-to-electron mass ratio. For $\tilde{V}_a \gg T_e$, we can expand the I_o modified Bessel function to obtain

$$\tilde{V}_a \simeq V_a - V_{fa} \ , \tag{2}$$

where

$$V_{fa} = (T_e/2) \ln (MT_e/4\pi^2 m V_a) \tag{3}$$

is the floating potential. For high voltage capacitive sheaths, $V_{fa} \ll V_a$ and $\tilde{V}_a \simeq V_a$. In this limit, we can relate the r.f. current density to the d.c. sheath voltage and sheath thickness:

$$J_a(\overline{x}) \propto V_a/s_a(\overline{x}) \ . \tag{4}$$

For a collisionless (Child law) sheath, we have[12,18]

$$n_{sa}(\overline{x}) \propto V_a^{3/2}/s_a^2(\overline{x}) \ ; \tag{5}$$

for a collisional (resonant charge transfer) sheath, we have[11,19,20]

$$n_{sa}(\overline{x}) \propto V_a^{3/2}/s_a^{5/2}(\overline{x}) \ ; \tag{6}$$

and for a collisional (elastic scattering) sheath, we have[14]

$$n_{sa}(\overline{x}) \propto V_a^2/s_a^3(\overline{x}) \ . \tag{7}$$

The total r.f. current I_a flowing to the powered electrode is

$$I_a \propto \int_{A_a} J_a(\overline{x}) \, d^2x \ . \tag{8}$$

Inserting (4) into (8) and using the collisionless sheath scaling to eliminate s_a, we obtain

$$I_a \propto V_a^{1/4} \int_{A_a} n_{sa}^{1/2}(\overline{x}) \, d^2x \ . \tag{9}$$

Similarly using the collisional sheath scalings (6) and (7) for resonant charge transfer or elastic scattering, we obtain, respectively,

$$I_a \propto V_a^{2/5} \int_{A_a} n_{sa}^{2/5}(\overline{x}) \, d^2x \tag{10}$$

and

$$I_a \propto V_a^{1/3} \int_{A_a} n_{sa}^{1/3}(\overline{x}) \, d^2x \ . \tag{11}$$

Similar expressions to (9) - (11) are obtained for the grounded electrode b. Equating I_a to I_b by conservation of r.f. current, we then obtain the fundamental scaling formula for high voltage sheaths,

$$\left[\frac{V_a}{V_b}\right]_0 = \left[\frac{\int_{A_b} n_{sb}^p(\bar{x})\, d^2x}{\int_{A_a} n_{sa}^p(\bar{x})\, d^2x}\right]^q , \tag{12}$$

where the exponents p and q are given in Table 1 for the three sheath scaling laws. We see that the voltage ratio is independent of the r.f. driving voltage and the electron temperature in the high voltage limit. The voltage ratio is determined by integrals over the powered and grounded areas that depend on the density at the plasma-sheath edge. This density is determined by the generation and loss processes for ions in the glow.

For large area ratios, the voltage across the large area electrode is low and the floating potentials in (2) cannot be neglected. This effect was also included in the study by Pointu[10]. The preceding analysis leading to (12) can be extended in a straightforward manner to obtain the relation

$$\frac{V_a}{V_b} = \left[\frac{1 - \dfrac{V_{fb}}{V_b}}{1 - \dfrac{V_{fa}}{V_a}} \frac{\int_{A_b} n_{sb}^p(\bar{x})\, d^2x}{\int_{A_a} n_{sa}^p(\bar{x})\, d^2x}\right]^q , \tag{13}$$

where now V_a and V_b must be related to the peak-to-peak r.f. voltage $\tilde{V}_{pp}$ applied to the discharge:

$$V_a + V_b = V_{fa} + V_{fb} + \tilde{V}_{pp}/2 . \tag{14}$$

Solving (13) and (14) numerically, we can obtain the voltage ratio V_a/V_b, which now depends on $\tilde{V}_{pp}$, T_e and M/m as well as the area integrals of the density. In the limiting case where $\tilde{V}_b = 0$, (1) yields $V_{fb} = (T_e/2)\ln(M/2\pi m)$ and (14) yields

$$\left[\frac{V_a}{V_b}\right]_{\max} \approx \frac{\tilde{V}_{pp}}{T_e \ln(M/2\pi m)} . \tag{15}$$

III. DIFFUSION IN THE GLOW

A. Finite Length Cylindrical Geometry

To determine the density in the glow at the plasma-sheath edge, we consider a simple transport model in which ions are generated at a rate $\nu_{iz} n$ proportional to the electron density and are lost by ambipolar diffusion to the walls with a constant diffusion coefficient D. The diffusion equation is

$$\nabla^2 n + (\nu_{iz}/D) n = 0 . \tag{16}$$

The general solution to (16) is

$$n = n_0 J_0(\alpha r) \cos(\beta z) , \tag{17}$$

where

$$\frac{\nu_{iz}}{D} = \alpha^2 + \beta^2 . \tag{18}$$

There are two approaches to the boundary conditions applied to the solution of (16). The first, which assumes that the mean free path λ_i is small compared with the chamber height and radius, specifies that n be zero on the walls of the chamber. The density at the sheath edge is then found by linearly extrapolating using the density slope at the wall. The second approach, which applies for larger values of λ_i, is to apply the general boundary condition specifying that the ion flow speed at the walls is normal to the wall and equal to u_B. This involves specifying the ratio of the local normal derivative of n to the value of n. This latter method is much more cumbersome and does not permit the compact expression for the surface integrals that can be obtained using the first method.

In the short mean free path approximation, α in (17) and (18) is just χ_{01}/R, where $\chi_{01} \simeq 2.405$ is the first zero of the zero order Bessel function J_0, and β is π/L. Given the geometry (L and R) and the diffusion constant D ($\simeq \lambda_i u_B$), then (18) determines the ionization rate ν_{iz}. Recalling that $\nu_{iz} = NK_{iz}$, where N is the neutral gas density and $K_{iz}(T_e)$ is the ionization rate constant, we see that (18) fixes T_e in the glow for a specified N.

The ion flux $n\overline{u}$ in the glow is given by

$$n\bar{u} = -D\,\nabla n\ . \tag{19}$$

Evaluating (19) at the plasma-sheath edge where $n = n_s$ and $|\bar{u}| = u_B$, we obtain

$$n_s(R,z) = \frac{n_0 D}{u_B}\frac{\chi_{01}\,J_1(\chi_{01})}{R}\cos(\pi z/L) \tag{20}$$

at the cylinder side and

$$n_s(r,\pm L/2) = \frac{n_0 D}{u_B}\frac{\pi}{L}\,J_0(\chi_{01} r/R) \tag{21}$$

at the cylinder top and bottom. Here J_1 is the first order Bessel function and $J_1(\chi_{01}) \simeq 0.5191$. Inserting (20) and (21) into (12) and doing the integrals for each of the three configurations in Figs. 1(a)-(c), we obtain the voltage ratios $(V_a/V_b)_0$ for each configuration in the limit of high sheath voltages. These can be written in terms of the two normalized functions

$$F_p(\zeta) = \int_0^{\zeta} d\zeta' \cos^p(\pi\zeta'/2)\ , \tag{22}$$

$$G_p(\zeta) = \int_0^{\zeta} \zeta'\, d\zeta' J_0^p(\chi_{01}\zeta')\ , \tag{23}$$

and the dimensionless geometric ratio

$$\rho_p = \frac{1}{2}\left[\frac{\chi_{01}\,J_1(\chi_{01})}{\pi}\right]^p \left[\frac{L}{R}\right]^{p+1}\ . \tag{24}$$

The functions F_p and G_p are shown in Fig. 2 for p = 1/3, 2/5, and 1/2. For $\zeta \ll 1$, $F_p \simeq \zeta$ and $G_p \simeq \zeta^2/2$. For $\zeta = 1$, $F_p = 2^p\,\Gamma^2((p+1)/2)/\pi\Gamma(p+1)$. The values of $F_p(1)$ and $G_p(1)$ are given in Table 1.

For the configuration of Fig. 1(a), we obtain using (22) and (23) in (12):

$$\left[\frac{V_a}{V_b}\right]_0 = \left[\frac{2\,G_p(1) - G_p(R_a/R)}{G_p(R_a/R)}\right]^q\ , \tag{25}$$

where p and q given in Table 1 depend on the assumed sheath physics. For the configuration of Fig. 1(b), we obtain

$$\left[\frac{V_a}{V_b}\right]_0 = \left[\frac{\rho_p^{-1}G_p(1) + F_p(1) + F_p(1-2H/L)}{\rho_p^{-1}G_p(1) + F_p(1) - F_p(1-2H/L)}\right]^q . \tag{26}$$

For the configuration of Fig. 1(c), we obtain

$$\left[\frac{V_a}{V_b}\right]_0 = \left[\frac{2G_p(1) + 2\rho_p F_p(1) - G_p(R_a/R)}{G_p(R_a/R)}\right]^q . \tag{27}$$

In order to solve for longer mean free paths cases ($\lambda_i \leq R, L/2$) and check the limits of validity of the short mean free path approximation, we assume that α and β are not equal to χ_{01}/R and π/L respectively, such that the boundary conditions using (14) become:

$$u_B = -(D/n)(\partial n/\partial r)\,|_{r=R} = D\,\alpha J_1(\alpha r)/J_0(\alpha r)\,|_{r=R} \tag{28}$$

at the cylinder side wall, and

$$u_B = -(D/n)(\partial n/\partial z)\,|_{z=L/2} = D\,\beta \sin(\beta z)/\cos(\beta z)\,|_{z=L/2} \tag{29}$$

at the top and bottom end walls. The solutions for α and β can be found as functions of λ_i/R and λ_i/L. The resulting values for α and β are found to be less than χ_{01}/R and π/L respectively, but approach these values for $\lambda_i \ll R$ or $L/2$. The solutions for dimensionless forms of α, $\alpha' = \alpha R/\chi_{01}$, and β, $\beta' = \beta L/\pi$, are shown in Fig. 3 as functions of λ_i/R and $2\lambda_i/L$.

B. Finite Length Coaxial Geometry

We consider a restricted class of coaxial geometries for which the inner and outer cylindrical walls (radii R_i and R_o) and the end walls are each undivided into powered or unpowered areas. Based on the accuracy of the short mean free path approximation for the finite cylindrical geometry, we solve the coaxial cylindrical discharge problem by linear extrapolation as in (20) and (21). In this case, the solution for n instead of using only J_0 for the radial dependence requires the Y_0's as well:

$$n = n_0[(J_0(kR)\,Y_0(kR_o) - Y_0(kr)\,J_0(kR_o))/Y_0(kR_o)]\cos(\pi z/L) . \tag{30}$$

In order to find the value of the ion density at the sheath edge, k in (30) is chosen such that $n = 0$ at the electrode surfaces. This yields the relation:

$$J_0(\gamma x)\,Y_0(x) - Y_0(\gamma x)\,J_0(x) = 0 , \tag{31}$$

where we have let $\gamma = R_i/R_o$ and $x = kR_o$ in (31), such that $\gamma x = kR_i$. Equation (31) can be solved numerically to obtain $\gamma(x)$. The expression (30) for n is then substituted into (19) with $u = u_B$. Assuming that the value of D/u_B is small, we get by linear extrapolation the value of n_s, the density at the sheath edge for the inner and outer electrode surfaces S_i and S_o and the end wall surfaces S_e. For the inner cylinder S_i, we obtain

$$n_s \propto k\,[Y_1(\gamma x)J_0(x) - J_1(\gamma x)Y_0(x)]\cos(\pi z/L)\,; \tag{32}$$

for the outer cylinder S_o, we obtain

$$n_s \propto k\,[-Y_1(x)J_0(x) + J_1(x)Y_0(x)]\cos(\pi z/L)\,; \tag{33}$$

and for each end wall S_e, we obtain

$$n_s \propto (\pi/L)\,[J_0(\zeta)Y_0(x) - Y_0(\zeta)J_0(x)]\,, \tag{34}$$

where $\zeta = kr$. The surface integrals are then found easily for each of the sheath types: Child-Langmuir, constant mean free path, and Cobine (constant mean free time), having p = 1/2, 2/5, and 1/3, respectively. For S_i,

$$\int_{S_i} n_s^p\,dz \propto (L/R_o^{p-1})X_p(\gamma)\,, \tag{35}$$

where

$$X_p(\gamma) = F_p(1)(\gamma x)^p\,[Y_1(\gamma x)J_0(x) - J_1(\gamma x)Y_0(x)]^p\,; \tag{36}$$

for S_o,

$$\int_{S_o} n_s^p\,dz \propto (L/R_o^{p-1})Y_p\,, \tag{37}$$

where

$$Y_p = F_p(1)x^p\,[-Y_1(x)J_0(x) + J_1(x)Y_0(x)]^p = (2/\pi)^p\,F_p(1)\,; \tag{38}$$

and for each end wall S_e,

$$\int_{S_e} n_s^p\,r\,dr \propto (\pi/L)^p R_o^2 Z_p(\gamma)\,, \tag{39}$$

where

$$Z_p(\gamma) = x^{-2} \int_{\gamma x}^{x} \zeta d\zeta \, [J_0(\zeta) Y_0(x) - Y_0(\zeta) J_0(x)]^p \ . \tag{40}$$

The constancy of Y_p follows from the Wronskian relation for the J and Y Bessel functions. The functions $X_p(\gamma)$ and $Z_p(\gamma)$ are shown in Fig. 4, and the values of Y_p are given in Table 1.

Let us introduce the dimensionless geometric ratio

$$\tau_p = \pi(L/\pi R_o)^{p+1} \ . \tag{41}$$

Then if both end walls are insulating and do not carry r.f. current, $(V_a/V_b)_0$ may be expressed very simply:

$$(V_a/V_b)_0 = (Y_p/X_p)^q \ , \tag{42}$$

where p and q are given in Table 1. If both end walls are conducting and part of the inner electrode a, the result is

$$(V_a/V_b)_0 = [Y_p/(X_p + \tau_p^{-1} Z_p)]^q \ . \tag{43}$$

If both end walls are conducting and part of the outer electrode b, then we have

$$(V_a/V_b)_0 = [(Y_p + \tau_p^{-1} Z_p)/X_p]^q \ . \tag{44}$$

IV. COMPARISON WITH EXPERIMENTS

The quantity measured in most experiments is the "bias ratio", defined as the bias voltage $V_{\text{bias}} = V_b - V_a$, normalized to the peak-to-peak r.f. voltage, which from (14) is $\tilde{V}_{pp} = 2(V_a + V_b - V_{fa} - V_{fb})$. Hence, we obtain

$$\frac{V_{\text{bias}}}{V_{pp}} \simeq \frac{1}{2} \frac{V_a/V_b - 1}{V_a/V_b + 1 - V_{fa}/V_b - V_{fb}/V_b} \ . \tag{45}$$

There have been relatively few bias ratio measurements done on low pressure ($\lesssim$100 mTorr) asymmetric capacitive r.f. discharges in which electrode areas and voltages were carefully controlled, and some of these were done in systems having electrodes whose areas were not very different [1,21]. The studies by Horwitz[8], Coburn and Kay[7], Kohler et al[6] and Yeom et al[9], however, have a sufficiently

wide range of area ratios and/or voltages to allow a meaningful comparison with the model presented here. We first compare the short mean free path model results with the measured biases, and later comment on the effects of finite mean free path on the model results.

Horwitz[8] has measured V_{bias}/V_{pp} at 13.56 MHz for the cylindrical geometries shown in Figs. 1(b) and (c) for various applied voltages V_{pp}, pressures, electrode materials, and gases. Figures 5 and 6, which are redrawn from Fig. 12 of ref. 8, show the measured results for the maximum of V_{bias}/V_{pp} (with respect to pressure) plotted against an "area ratio". The four sets of points B, C, D, and E at the largest area ratios are for the geometry of Fig 1(b) with $R \approx 10.35$ cm, $L \approx 5.3$ cm, and $H \approx 0$, 1, 2, and 3 cm, respectively. The set of points A at the smallest area ratio is for the geometry of Fig. 1(c) with $R \approx 13.4$ cm, $L \approx 5.3$ cm, and $R_a \approx 10.2$ cm. Horwitz found that V_{bias}/V_{pp} was only weakly dependent on the pressure, displaying a broad maximum with respect to pressure, and was only weakly dependent on the type of gas and the electrode material. The points plotted in Figs. 5 and 6 are typically for pressures of 4-12 mTorr.

To compare these data with the model of Sec. III, we choose a typical electron temperature $T_e \approx 5$ eV in argon gas. Then the model results are shown in Fig. 5 for Child law sheaths and in Fig. 6 for constant mean free path sheaths. The ion mean free paths in argon are 0.4-1.3 cm, of the order of the typical sheath thickness. Thus we are in a collisional transition regime between these two sheath models. For argon, resonant charge transfer dominates over elastic scattering; hence the constant mean free path model is more appropriate than the constant mean free time (Cobine) model. The open triangles in Figs. 5 and 6 show the high voltage sheath results using (12) in (45) with $V_{fa} = V_{fb} = 0$. We see that the high voltage results generally follow the measured results at $V_{pp} = 1400$ V, although there is a significant deviation at the lowest area ratio for Child law sheaths. The pluses and open circles show the model results obtained using (3), (13) and (14) in (45) to determine V_{bias}/V_{pp}, numerically, for $V_{pp} = 330$ V and 1400 V, respectively. Both the Child law and constant mean free path sheath results are in good agreement with the measurements, giving not only the correct dependence on geometry but also the correct voltage dependence. The model also predicts that V_{bias}/V_{pp} should be independent of pressure, electrode material, and (except for a weak, logarithmic dependence on M/m) type of gas, in agreement with the measurements. However, changing these parameters can change T_e, which would

yield a weak variation of the model results at low driving voltages. To predict the variation of T_e with these parameters, however, is beyond the scope of our model.

Coburn and Kay[7] have directly measured V_b/V_a at 13.56 MHz for the cylindrical geometry shown in Fig. 1(a) for various applied r.f. voltages in an argon discharge at 50 mTorr. They found that for high r.f. voltages on the powered electrode, V_b scaled approximately linearly with V_a,

$$V_b \simeq K_1 V_a + K_2 , \tag{46}$$

where K_1 depended on the geometry ("area ratio") and K_2 was roughly a constant, independent of geometry. Figure 7, which is redrawn from Fig. 5 of ref. 7, shows the measured results for V_b versus V_a. The five curves A-E are in order of increasing "area ratio" for $R_a \simeq 2.54$ cm, $L \simeq 1.88$ cm, and $R \simeq 2.95$, 3.5, 4.25, 4.75, and 5.3 cm, respectively.

To see that (13) yields an expression in the form (46), we expand (13) in the limit $V_{fa} \ll V_a$ to obtain

$$V_b \simeq (V_b/V_a)_0 V_a + q\, V_{fb} , \tag{47}$$

where $(V_b/V_a)_0$ is given by (12) and V_{fb} by (3) with $a \to b$. We note from (3) that V_{fb} is a constant, to within a weak logarithmic factor. Comparing (47) and (46), we have $K_1 = (V_b/V_a)_0$. However, for the range of V_b's shown in Fig. 7, the higher order terms in the expansion leading to (47) are important, and there is a departure from linearity.

To compare the data in Fig. 7 with the model of Sec. III, we choose a typical electron temperature $T_e \simeq 4$ eV in this 50 mTorr argon discharge. One further choice must be made. For the geometry of Fig. 1(a), leading to $(V_b/V_a)_0$ given by (25), the r.f. current flowing to the grounded electrode through the insulating side wall cylinder was taken to be zero. Actually, some r.f. current must flow through this side wall by virtue of its capacitance to the grounded surfaces outside. To account for this effect, we have increased the radius of the cylinder by a somewhat arbitrary amount ΔR, choosing $R' = R + \Delta R$ with $\Delta R = 0.25$ cm.

Figure 7 shows the constant mean free path sheath results using (3) in (19) and (20) to obtain V_b versus V_a for $V_{pp} =$ 500, 800, and 1400 V. At 50 mTorr, there are from several to ten ion mean free

paths in a typical sheath thickness, and so this collisional model is more appropriate than the Child law model. There is good agreement between the collisional model and the measurements except at the highest "area ratios", where the model deviates somewhat from the measurements. For these cases, almost all of the applied r.f. voltage is dropped across the powered sheath, and the grounded electrode sheath is in the transition regime $\bar{V}_b \sim V_{fb} \sim 5T_e$. We do not expect this low voltage sheath to be described well by the approximate forms given in (2)-(7). Furthermore, there may be a mixed collisionality regime in which the ion motion in the (thin) grounded sheath is collisionless, while the motion in the (thick) powered sheath is collisional. Overall, the agreement between the model and the measurements is satisfactory for the regime in which the model is valid.

In contrast, a similar comparison of the model and data for Child law sheaths is not as good. To illustrate this, we reproduce in Fig. 8, redrawn from Fig. 6 of ref. 7, the slopes K_1 of the lines shown in Fig. 7, plotted against an "area ratio". The predictions of the constant mean free path model (solid dots) are seen to fit the data much better than the predictions of the Child law sheath model (solid squares). The sensitivity of the model to changes in ΔR is also illustrated in Fig. 8 for the cases of data points B and E. The upper bound is for $\Delta R = 0$ and the lower bound is for $\Delta R = 0.5$ cm.

Kohler et al[6] have measured V_{bias}/V_{pp} for a 20 mTorr argon discharge in the cylindrical geometry shown in Fig. 1(c), for which the powered electrode was one end wall and the grounded electrode was the other end wall and the cylinder side, with $R = R_a \simeq 7.95$ cm and $L \simeq 6.3$ cm. Measurements for this "confined" geometry[6] were made over a range of V_{pp} from 400 to 1700 volts. The measured results for V_{bias} versus V_{pp} are shown as the open triangles in Fig. 9, which is redrawn from Fig. 8 of ref. 6. Kohler et al also measured the temperature to be $T_e \simeq 3.2$ eV. The model results are obtained using (3), (13) and (14) in (45) to determine V_{bias} for $V_{pp} = 400$, 1000, and 1600 volts. The solid dots are the results for Child law sheaths, and the open circles are for constant ion mean free path sheaths. We see that there is good agreement between the measurements and both model results in this collisionally transitional pressure regime.

Yeom et al[9] have measured V_{bias}/V_{pp} for a 3 mTorr argon discharge in a finite coaxial geometry for which the inner cylindrical wall is the powered electrode and the outer cylindrical wall and the two

end walls are the grounded electrode. Although most of their measurements were in cylindrical magnetron geometry, having a d.c. axial magnetic field B, they also report some measurements for $B = 0$. For this system, $R_o \approx 10.5$ cm, $L \approx 18.16$ cm, and measurements were made for three different inner cylinder radii $R_i \approx 5.0$, 1.27, and 0.635 cm. The results for V_{bias}/V_{pp}, taken from Fig. 2 of ref. 13, are shown in the second column of Table 2. Yeom et al state that the measured electron temperature from Langmuir probes is approximately 12 eV. However, such measurements are notoriously difficult to make in capacitive r.f. discharges[22]. It seems unlikely that such large temperatures can be sustained in a 13.56 MHz discharge at $B = 0$. We therefore compare the measurements to the model using both the measured $T_e \approx 12$ eV and a more reasonable value of $T_e \approx 5$ eV. Also, Yeom et al do not directly give the driving voltage V_{pp} for the data in their Fig. 2, but instead specify an r.m.s. current density $J_{rms} = 6.0$ mA/cm^2. Subsequently, they present measurements showing that $V_{pp} \approx 275$ V at $J_{rms} = 3$ mA/cm^2 and $B = 200$ G. Lacking any better estimate, we choose $V_{pp} \approx 550$ V for $J_{rms} = 6.0$ mA/cm^2 and $B = 0$. Using these values of T_e and V_{pp}, we solve (13) and (14) numerically for V_a and V_b using (44) for the ratio of the integrals in (13). We then evaluate V_{bias}/V_{pp} from (45) to obtain the results in columns 3 through 6 of Table 2 for both Child law sheaths and constant mean free path sheaths. These model results are in good agreement with the measured values in column 2.

When the charge exchange mean free path λ_i is a significant fraction of the interelectrode gap or cylinder radius, there may be a need to calculate the density n_s at the sheath edge more precisely than the linear approximation of (20) and (21). The technique used is to obtain values of α and β by solving (28) and (29) [See Fig. 3] and insert these values in (17) to determine n. This density is then integrated over the electrode and wall surfaces as in (12) for $r = R$ or $z = \pm L/2$ to yield values for $(V_a/V_b)_0$. These are shown in Fig. 10 as functions of the mean free path normalized to half the interelectrode gap. In most situations, especially for small electrode area ratios, and for all cases using the constant mean free path sheath model, the change in $(V_a/V_b)_0$ for $2\lambda_i/L = 0.2$ (which corresponds to about 12 mTorr in refs. 6 or 8) is less than 10%. Thus we justify using the short mean free path limit model results in comparing with the experimental measurements.

V. DISCUSSION AND CONCLUSION

Starting from the crucial observation that the glow-to-electrode voltage across each sheath is a constant, independent of position along the sheath surface, we were able to decouple the equations for the sheath and glow dynamics in the high sheath voltage limit. For the sheath dynamics, we treated a collisionless (Child law) model and two collisional models, one having constant ion mean free path in the sheath and one having constant ion mean free time. For the glow dynamics, we treated finite length cylindrical and coaxial geometry, with plasma generation having a volume ionization rate proportional to the electron density and with plasma loss to the walls by ambipolar diffusion with a constant diffusion coefficient. Separately solving the equations for the sheath and glow and then combining the results, we obtained the powered-to-grounded electrode voltage ratio as the ratio of integrals over the powered and grounded areas of certain powers of the known density at the plasma-sheath edge. Hence, the voltage ratio was shown not to be determined as a simple power of the electrode area ratio, as is commonly assumed. These results were extended to low voltage sheaths using approximate expressions for the d.c. floating potentials at the sheaths, and were extended to include finite mean free path effects in the glow. Formulae and graphs were obtained allowing the voltage ratio to be found for any finite cylindrical geometry and for a restricted class of finite coaxial geometries.

The model results were then compared to four published experimental studies of the voltage ratio, three in finite cylindrical geometry and one in finite coaxial geometry. In all cases, we found good agreement between the model results and the measurements. The model successfully predicts the dependence of the voltage ratio on the discharge geometry and driving voltage. The model also predicts that there should be little dependence of the voltage ratio on the type of gas and the electrode material, in agreement with experimental measurements. The collisionless (Child law) sheath model agrees best with measurements at low pressures, and the collisional (constant ion mean free path) sheath model agrees best at higher pressures. However, within a given sheath collisionality regime, the model predicts little dependence of the voltage ratio on the discharge pressure, again in agreement with the experimental measurements.

We believe there are several reasons for the closer agreement of our model with the measurements of refs. 6-9 than previous models in the literature. The first, and most apparent, is the two dimensionality of our model. The effect of this on the sheath impedances at the electrodes is caused by the large variation over the top or side walls of the plasma density n_s at the sheath edge. Radial and axial dependences of this density, found from (21) and (20), are seen to be quite different from each other, and vary by large factors over the electrode and wall surfaces. As a result, the ion current density varies significantly over the walls and thereby causes the sheath thickness and capacitive impedance to vary as $n_s^{-1/2}$ (Child law) or $n_s^{-2/5}$ (constant mean free path). We have calculated the average values of n_s over the powered and grounded electrode surfaces in order to determine the ratio of the average current densities. This is shown in Fig. 11. Two immediate conclusions may be drawn: First, the average current density j_a at the smaller electrode is at least 40% greater than j_b for electrode area ratios of 2 to 3. This flatly contradicts the often used assumption that j_a and j_b are equal. Second, the geometry (aspect ratio R/L) also affects the dependence of j_a/j_b on area ratio. This is intuitively evident since it can be seen from (20) and (21) that n_s at the side wall relative to n_s at the top and bottom walls will be strongly affected by aspect ratio.

A second reason for the closer agreement between our model and experiment is the incorporation, as in Pointu[10], of the floating potential, which causes sheath capacitances to be more accurately approximated in the large area ratio or low voltage cases. A third reason is our use of a collisional sheath model in the higher pressure regimes.

The areas in which our model may not reflect the physics of some experiments with precision include both sheath and bulk plasma effects. Firstly, the ionization may not be strictly proportional to n due to thermal gradients or secondary electron generation at the electrode surfaces. This is apt to happen more at high pressures ($\gtrsim$ 200 mTorr) or in very large systems ($R, L \gtrsim 1$ m). The neglect of the electrical resistance of the glow region may also be inappropriate in these cases. At more moderate pressures, stochastic heating by the oscillating sheaths may also lead to strongly nonuniform ionization profiles[11,18,20]. Furthermore, the solution for n in (16) has been found by assuming ν_{iz}/D is constant over the plasma volume. This is not correct since the diffusion coefficient D is actually inversely proportional to the flow speed u for charge exchange collisions in the glow, and u varies spatially within

the glow[4,11]. This approximation will be relaxed in an upcoming numerical study. Lastly, we have neglected the sheath thicknesses in calculating the electrode areas. This might be most significant in the case of the Coburn and Kay experiment[7].

This work was supported in part by National Science Foundation Grant ECS-8517363, Department of Energy Grant DE-FG03-87ER13727, and a gift from Applied Materials, Inc. Helpful discussions with C.K. Birdsall and A.J. Lichtenberg are gratefully acknowledged.

REFERENCES

1. H.R. Koenig and L.I. Maissel, *IBM J. Res. Dev.* **14**, 168 (1970).

2. J.L. Vossen, *J. Electrochem. Soc.* **126**, 2345 (1979).

3. V.A. Godyak, *Sov. J. Plasma Phys.* **2**, 78 (1976).

4. V.A. Godyak, *Soviet Radio Frequency Discharge Research*, (Delphic Associates, Inc., Falls Church, VA), pp. 110-113 (1986).

5. B. Chapman, *Glow Discharge Processes*, Wiley, New York (1980).

6. K. Kohler, J.W. Coburn, D.E. Horne, E. Kay, and J.H. Keller, *J. Appl. Phys.* **57**, 59 (1985).

7. J.W. Coburn and E. Kay, *J. Appl. Phys.* **43**, 4965 (1972).

8. C.M. Horwitz, *J. Vac. Sci. Technol. A* **1**, 60 (1983).

9. G.Y. Yeom, J.A. Thornton, and M.J. Kushner, *J. Appl. Phys.* 65, 3825 (1989).

10. A.M. Pointu, *Appl. Phys. Lett.* 50, 1047 (1987).

11. M.A. Lieberman, *J. Appl. Phys.* 65, 4186 (1989).

12. S.E. Savas, *Mat. Res. Symp. Proc.* 98, 35 (Apelian and Szekely, eds., Pittsburgh, PA, 1987).

13. C.D. Child, *Phys. Rev.* **32**, 492 (1915).

14. J.D. Cobine, *Gaseous Conductors*, Dover, New York, p. 128 (1941).

15. F.F. Chen, *Introduction to Plasma Physics and Controlled Fusion*, Plenum Press, New York, 1984, p. 292.

16. Reference 4, p. 86.

17. A. Garscadden and K.G. Emeleus, *Proc. Phys. Soc. (London)* 79, 535 (1962).

18. M.A. Lieberman, *IEEE Trans. Plasma Sci.* **PS-16**, 638 (1988).

19. R.S. Morgan, *Plasma Etching in Semiconductor Fabrication*, Elsevier, New York, 1985, p. 230.

20. M.A. Lieberman, *IEEE Trans. Plasma Sci.* PS-17, 338 (1989).

21. A.J. van Roosmalen, W.G.M. van den Hoek, and H. Kalter, *J. Appl. Phys.* 58, 653 (1985).

22. V.A. Godyak, "Langmuir Probe Diagnostics in RF Plasma (A Critical Review)", Report E-23, 41st Annual Gaseous Electronics Conference, Minneapolis, MN, October 17-21, 1988.

Table 1. Exponents and function values for various sheath scaling laws.

Sheath Ion Transport	p	q	$F_p(1)$	$G_p(1)$	Y_p
Collisionless	$\frac{1}{2}$	4	0.3808	0.1518	0.608
Elastic Scattering	$\frac{1}{3}$	3	0.4103	0.1744	0.706
Resonant Charge Transfer	$\frac{2}{5}$	$\frac{5}{2}$	0.3978	0.1647	0.664

Table 2. Comparison of measurements and model in finite coaxial geometry.

R_i (cm)	V_{bias}/V_{pp}				
	Measured	Child's law		Const m.f.p. law	
		T_e = 5 eV	T_e = 12 eV	T_e = 5 eV	T_e = 12 eV
5.0	0.285	0.355	0.28	0.315	0.27
1.27	0.42	0.44	0.375	0.44	0.395
0.635	0.425	0.44	0.375	0.45	0.405

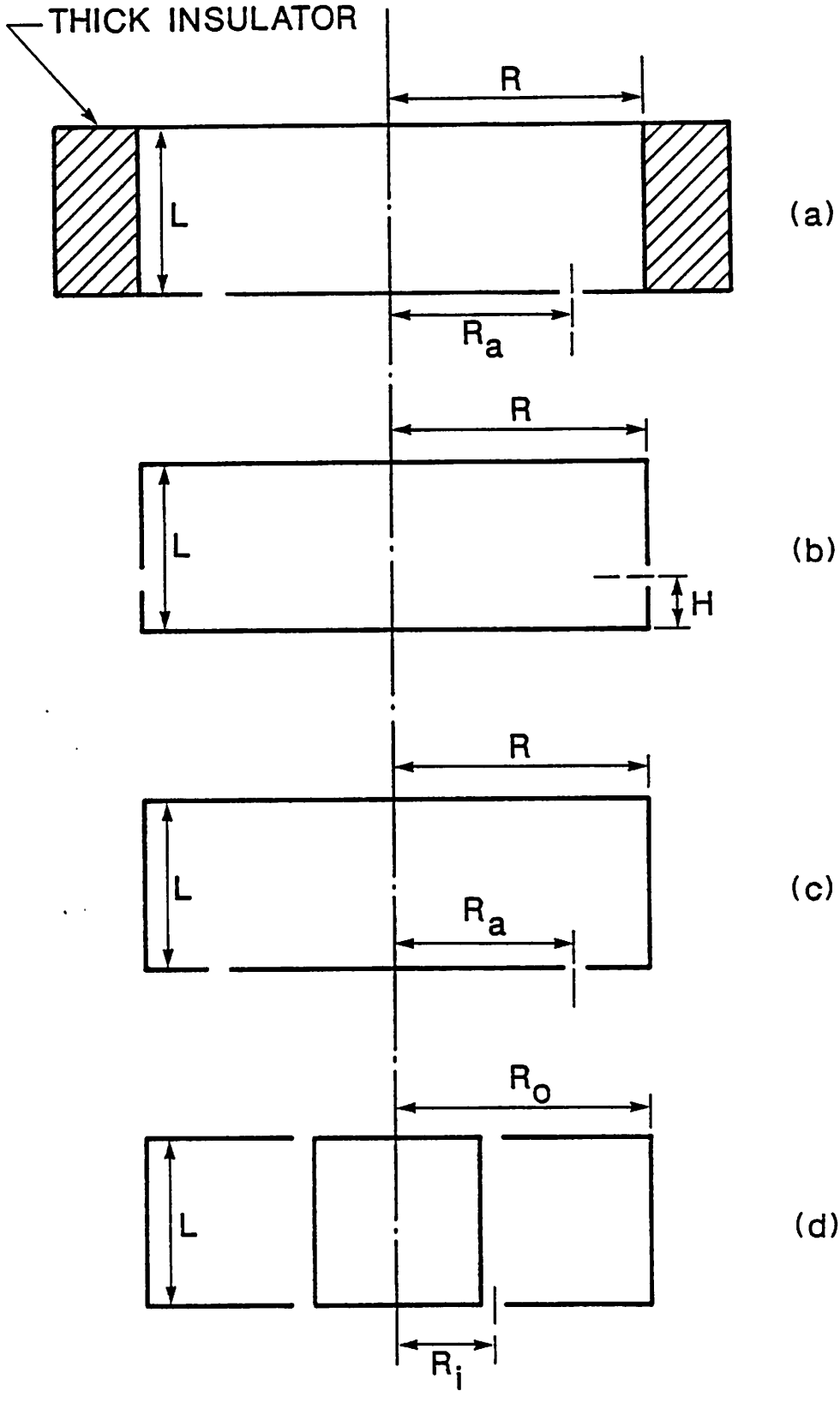

Fig. 1. Geometry of the basic discharge configurations.

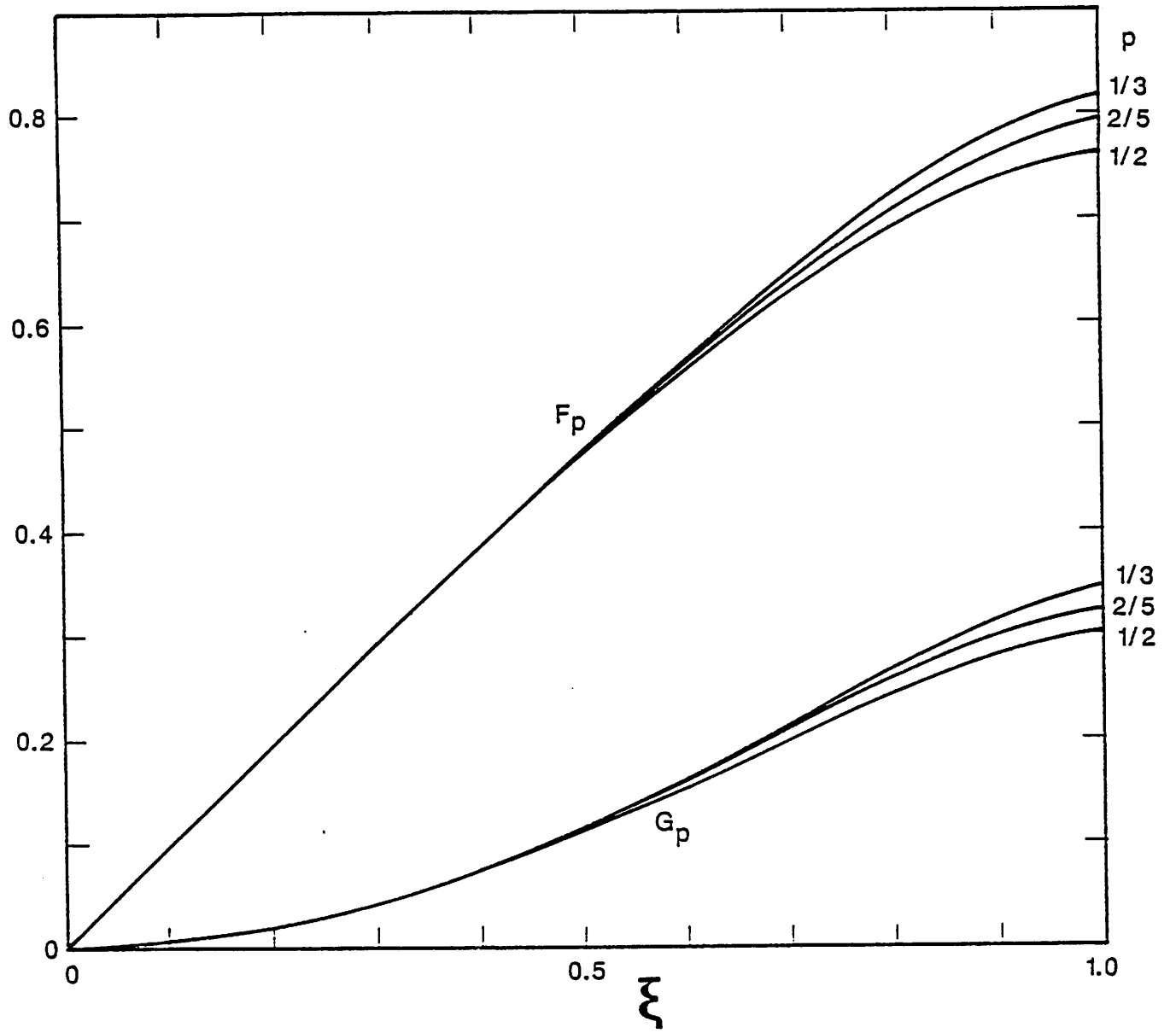

Fig. 2. F_p and G_p versus ζ for $p = 1/3, 2/5$, and $1/2$.

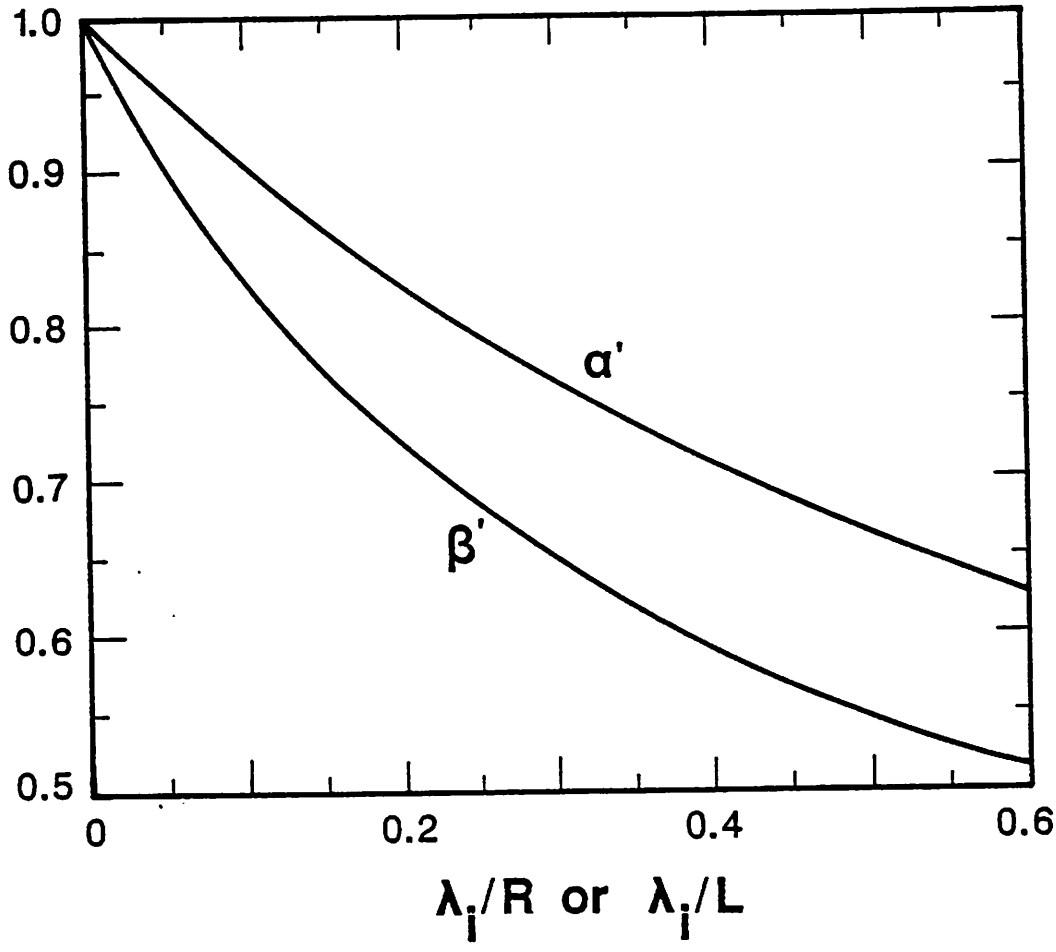

Fig. 3. α' versus λ_i/R and β' versus $2\lambda_i/L$.

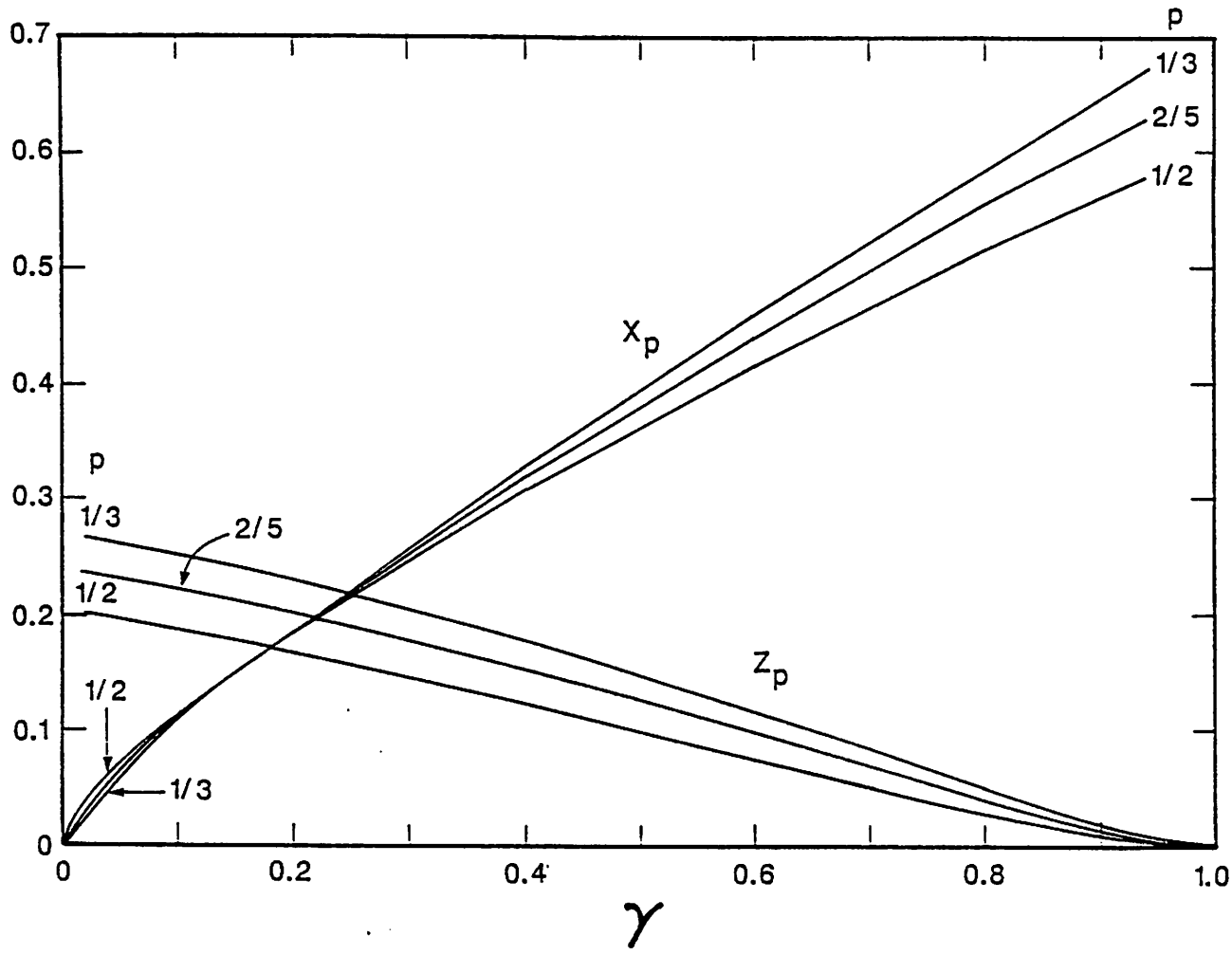

Fig. 4. X_p and Z_p versus γ for p = 1/3, 2/5, and 1/2. The value of Y_p is given in Table 1.

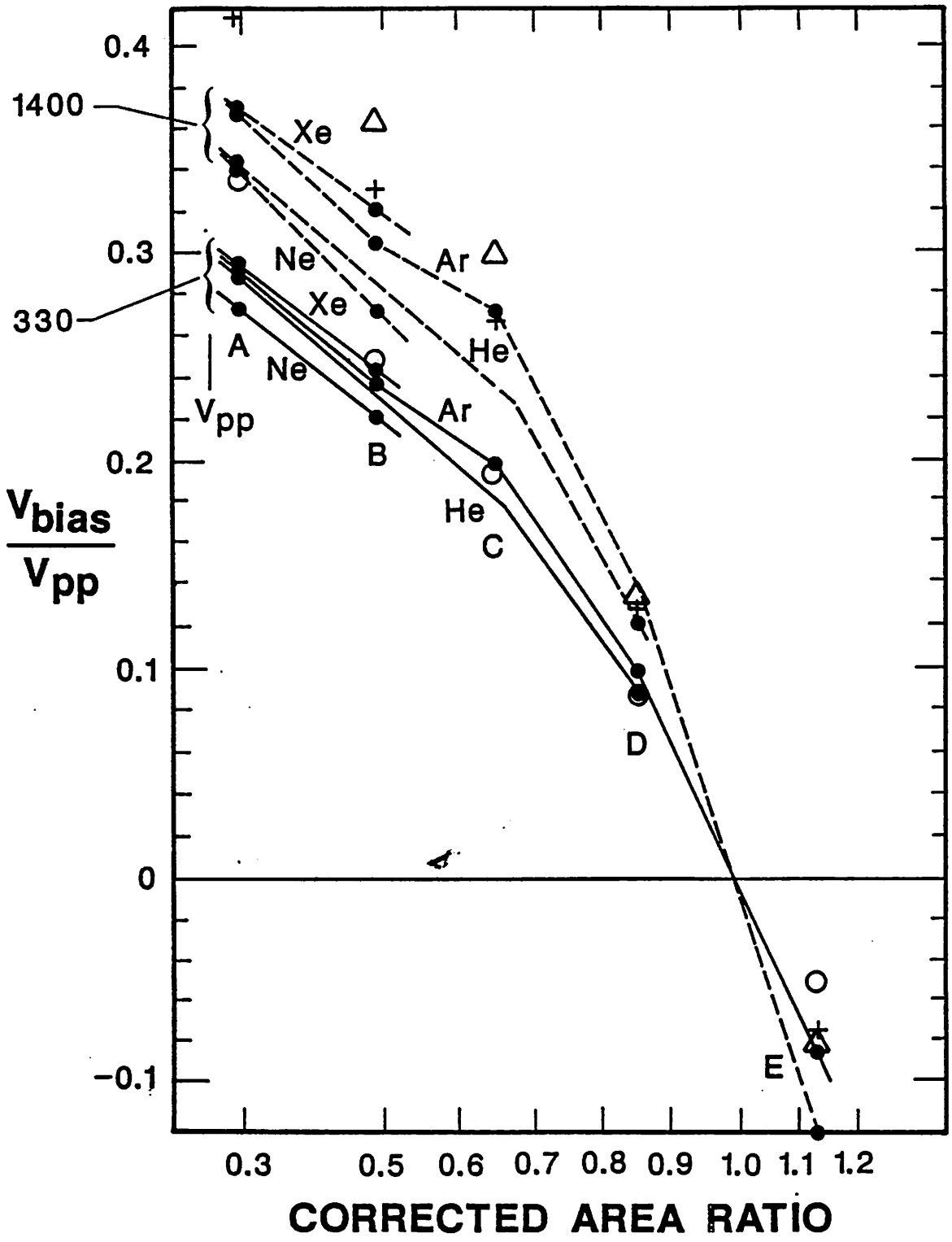

Fig. 5. Measurements of V_{bias}/V_{pp} versus "area ratio", redrawn from Fig. 12 of reference 8, along with the model results using Child law (collisionless) ion sheaths. The open triangles show the high voltage sheath model results. (The point for case A at $V_{bias}/V_{pp} \approx 0.46$ is off of the figure.) The pluses and open circles show the model results for V_{pp} = 1400 and 330 V, respectively.

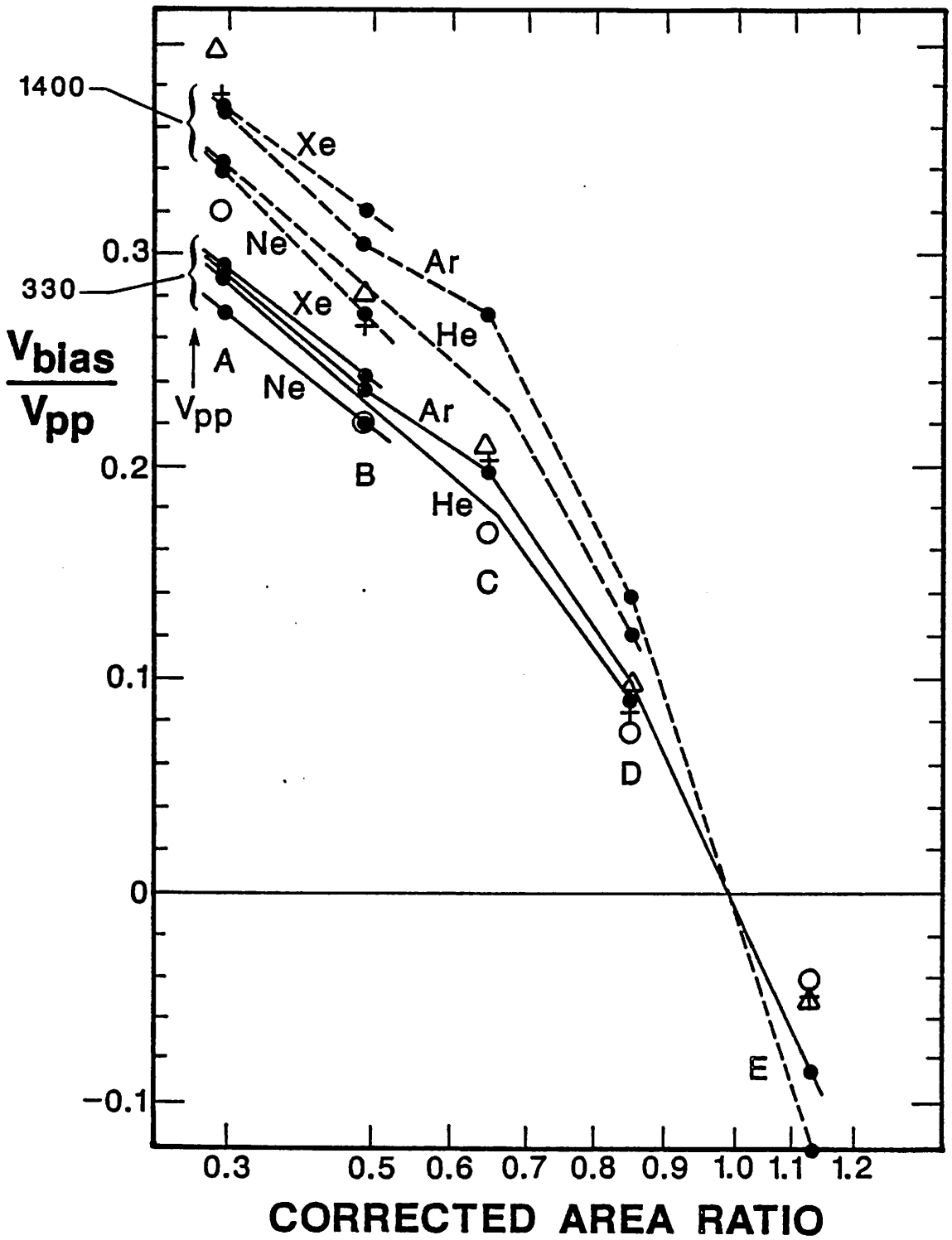

Fig. 6. Measurements of V_{bias}/V_{pp} versus "area ratio", redrawn from Fig. 12 of reference 8, along with the model results using constant mean free path collisional ion sheaths. The open triangles show the high voltage sheath model results. The plusses and open circles show the model results for V_{pp} = 1400 and 330 V, respectively.

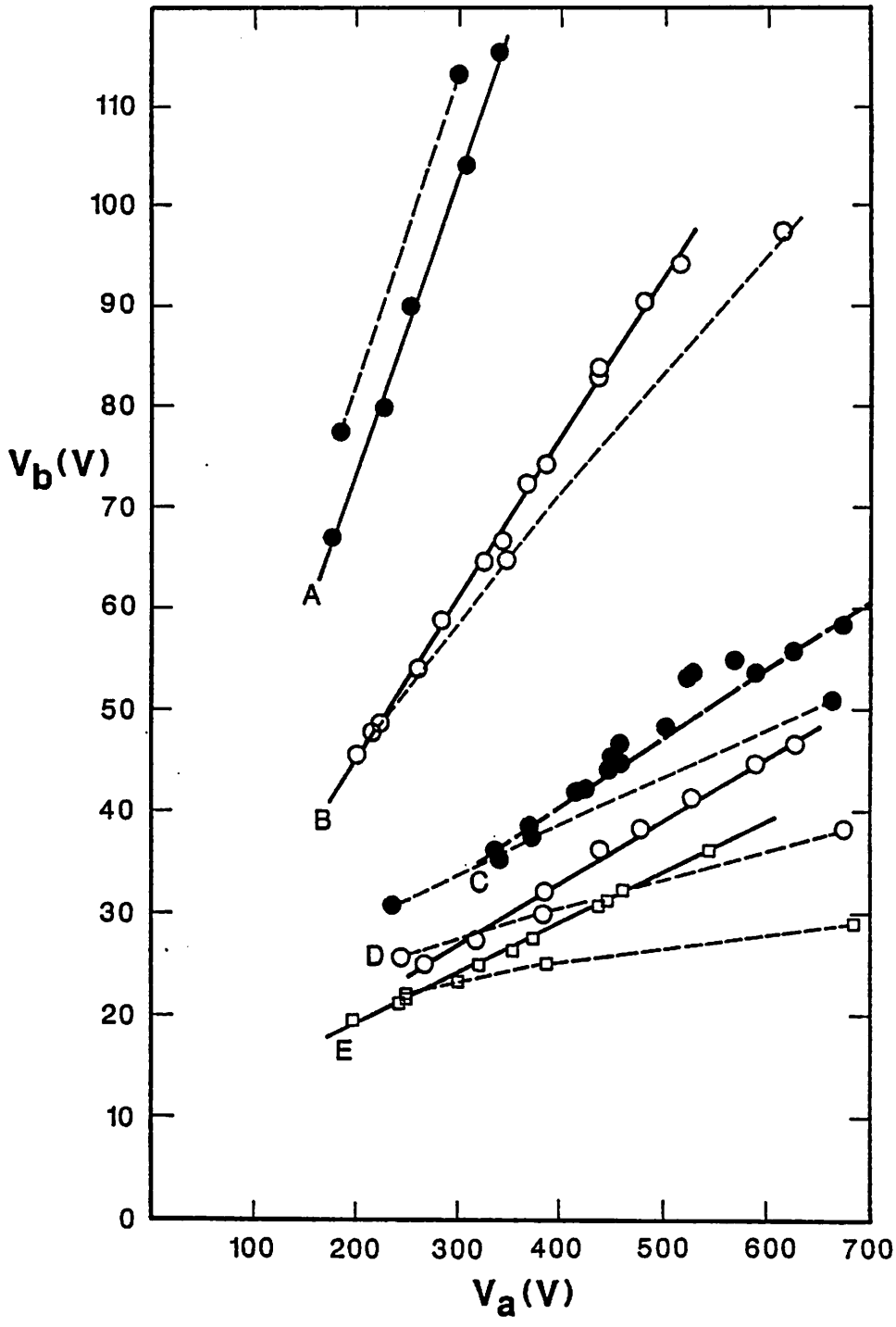

Fig. 7. Measurements of V_b versus V_a for five "area ratios", redrawn from Fig. 5 of reference 7, along with the model results (dashed lines) using the constant ion mean free path sheath model, with ΔR = 0.25 cm.

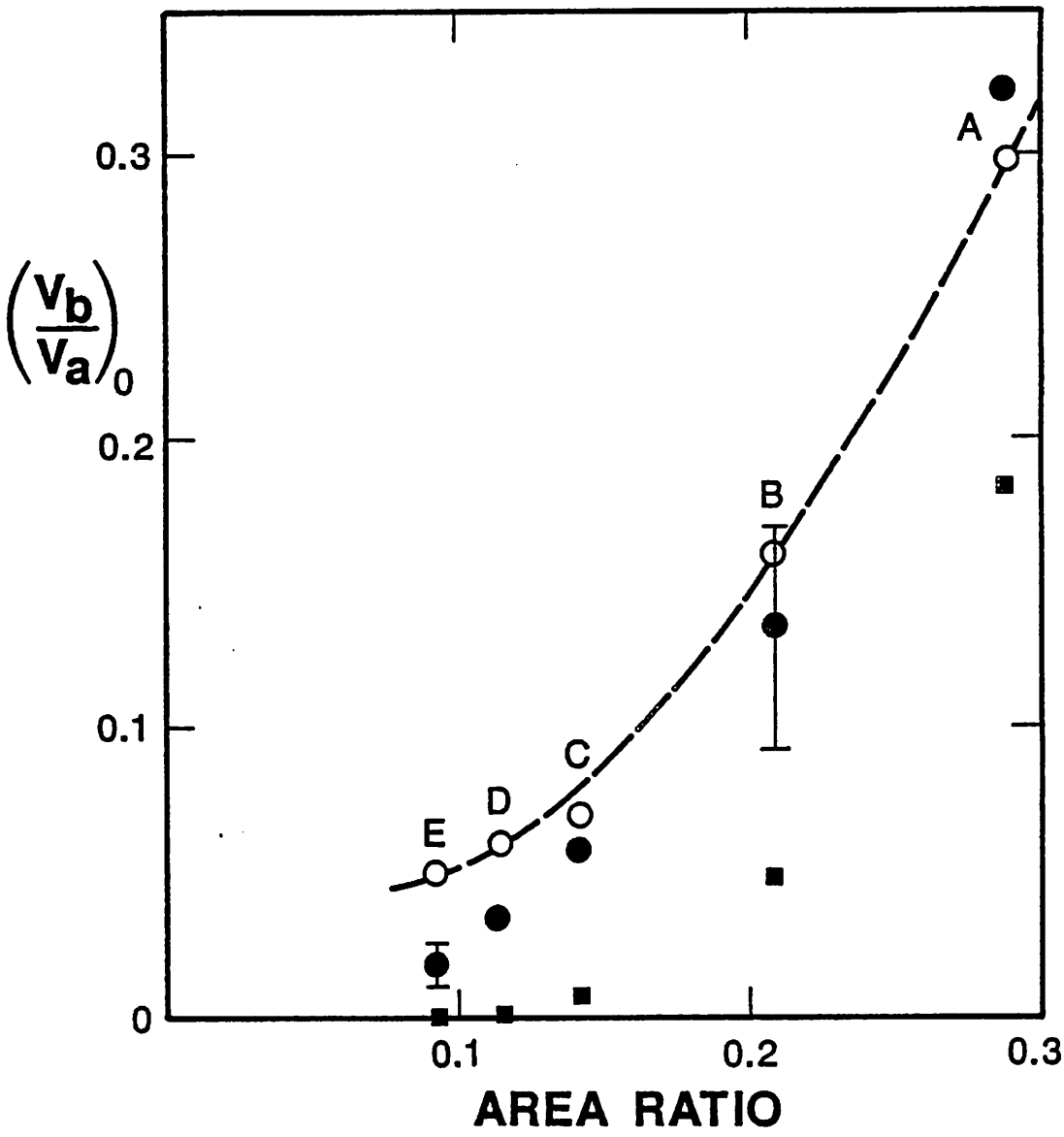

Fig. 8. Values of the slopes K_1 of the measured curves shown in Fig. 7, redrawn from Fig. 6 of reference 7, along with the model results for $(V_b/V_a)_0 = K_1$. The solid dots are for the constant ion mean free path sheath model, and the solid squares are for the Child law sheath model. The lower and upper bounds shown for cases B and E show the sensitivity of the model results to changes in the cylinder radius R.

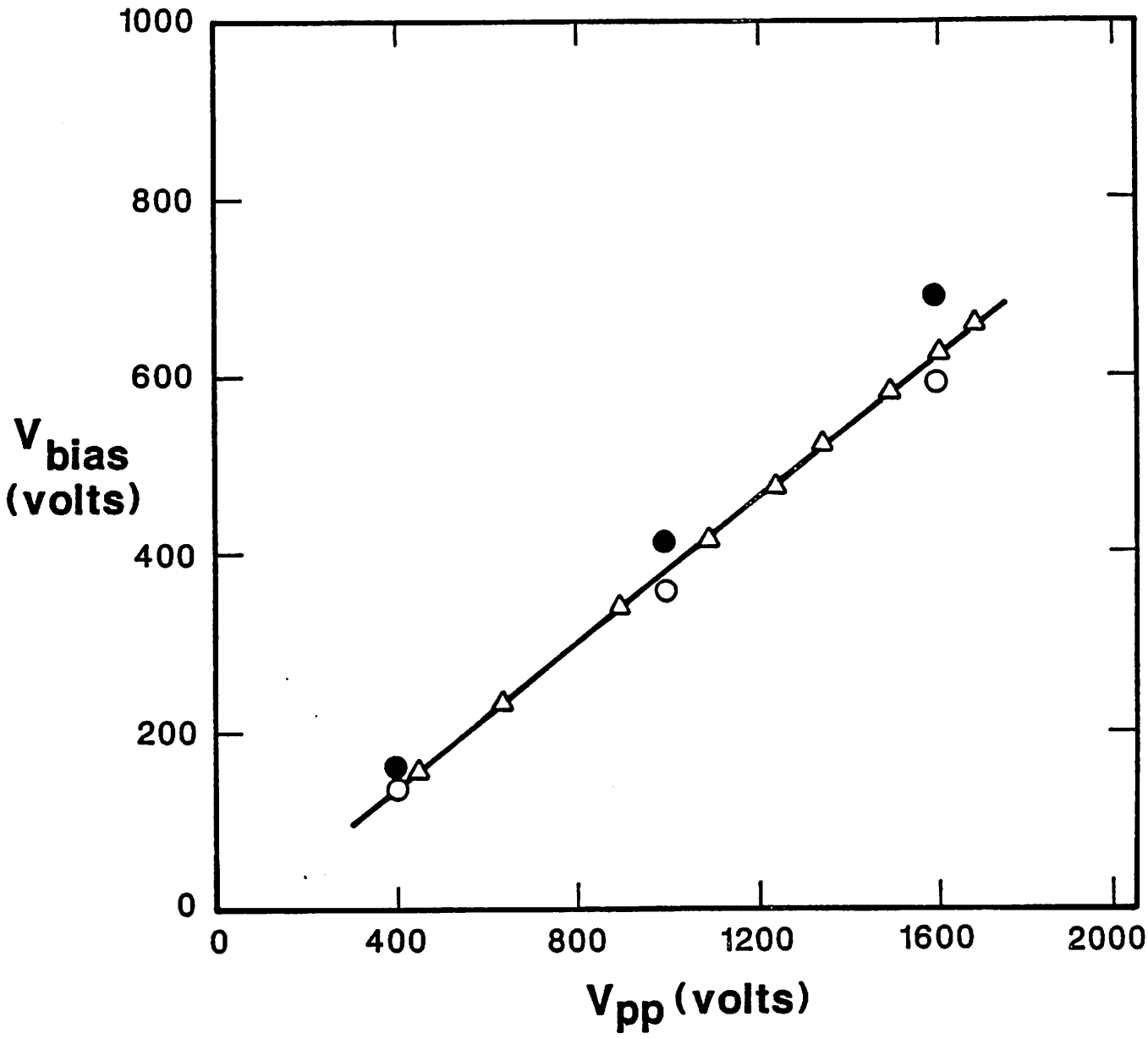

Fig. 9. Measurements of V_{bias} versus V_{pp} for a "confined" r.f. discharge, redrawn from Fig. 8 of reference 6. The open triangles are the measured values, and the closed and open circles are the model results for Child law sheaths and constant ion mean free path sheaths, respectively.

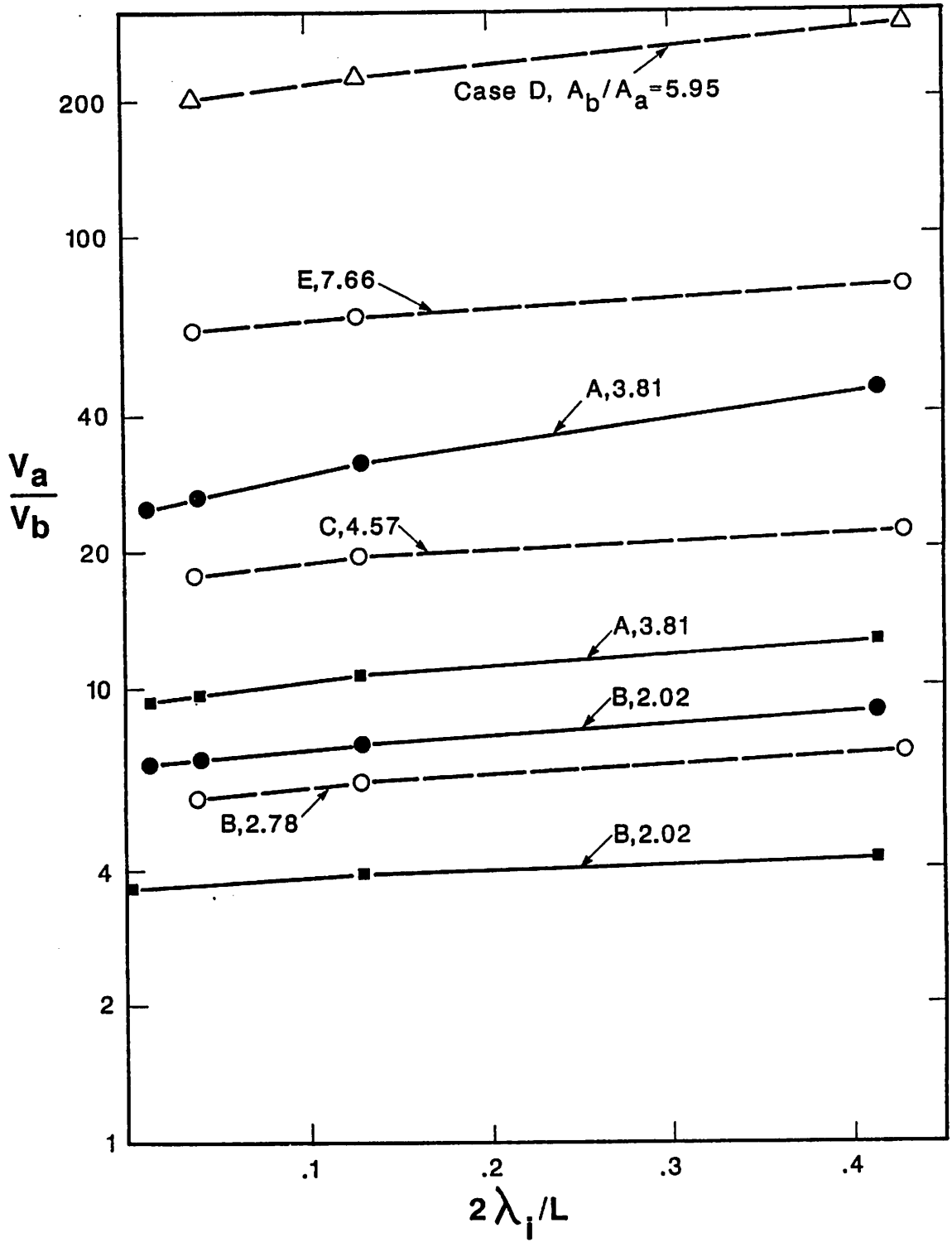

Fig. 10. V_a/V_b versus $2\lambda_i/L$ for various cases having area ratios A_b/A_a. The solid dots and squares are the model results for the Horwitz data of reference 8 using Child law sheaths and constant ion mean free path sheaths, respectively. The open circles and triangles are the corresponding model results for the Coburn and Kay data of reference 7.

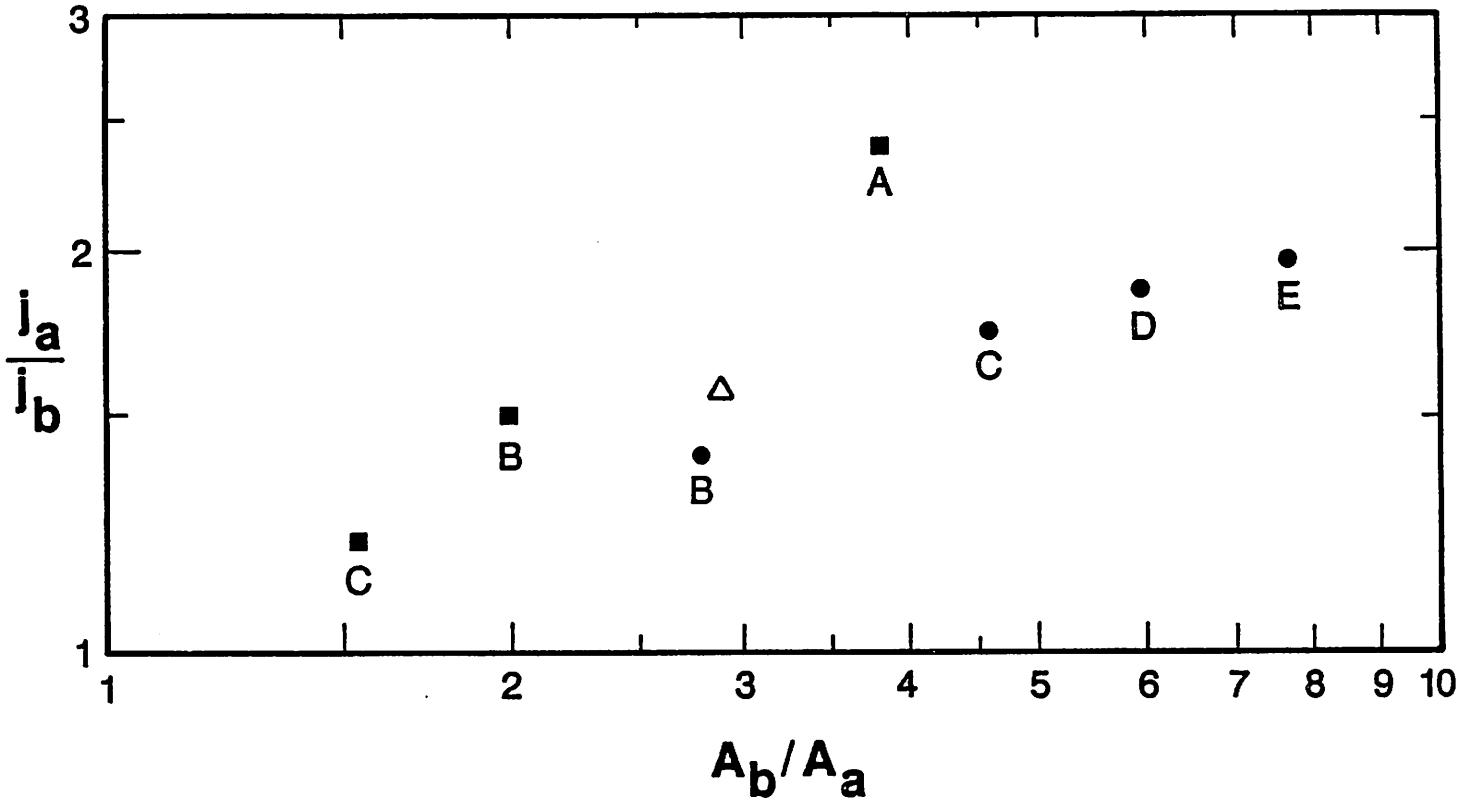

Fig. 11. Ratio of d.c. ion current densities j_a/j_b versus ratio of areas A_b/A_a in the model for the data of Coburn and Kay (solid dots), Kohler et al (open triangle) and Horwitz (solid squares).